ChemCatChem

Research Article
doi.org/10.1002/cctc.202201489

Chemistry Europe
European Chemical Societies Publishing

www.chemcatchem.org

Special Collection

Plugging the ^{3}MC Sink in Ru^{II}-Based Photocatalysts

Georgina E. Shillito,[a] Sven Rau,[b] and Stephan Kupfer*[a]

Quantum chemical methods have been utilised to explore the kinetics and thermodynamics of a prominent charge recombination pathway in a series of Ru^{II} based molecular photocatalysts. Selective tuning of the Ru^{II} coordination sphere, replacing the tbbpy ligands of the hydrogen evolving parent photocatalyst with electron rich, biimidazole based ligands, promotes unidirectional charge transfer towards the bridging ligand during initial photoexcitation. These electronic effects are also significant in the triplet manifold, where the predicted rate of the undesired deactivation process from the ^{3}MLCT state on the bridging ligand to a ^{3}MC state on the ruthenium centre, is decreased relative to the parent complex, by 1–2 orders of magnitude, alongside a decrease in electronic coupling. This design methodology could be utilised to promote targeted (light-driven) electron transfer pathways, as well as to potentially reduce ^{3}MC deactivation pathways in commonly used polypyridyl-based Ru^{II} photocentres, thus enhancing the quantum efficiency of light driven catalysis.

Introduction

A greater understanding of the fundamental interactions between light and photoactive molecules has facilitated the improved development of nature-inspired, synthetic, light-harvesting materials for a range of applications. The pressing need for clean, renewable energy has helped to drive research in the field of molecular electronics and the pursuit of efficient photoactive materials.

The generation of hydrogen via the use of molecular photocatalysts is one such area of research with growing interest.[1] Intramolecular photocatalysts in which the light-absorbing and catalytic centres are linked, often via an electron bridging group to form a single component supramolecular photocatalyst avoid problems associated with diffusion between the photosensitising and catalytic components. One such supramolecular motif, $[(tbbpy)_2Ru(tpphz)PdCl_2]^{2+}$ (where tbbpy = 4,4′-di-tert-butyl-2,2′-bipyridine and tpphz = tetrapyrido[3,2-a:2′,3′-c:3‴′-h:2‴′,3‴′-j]phenazine) introduced by Rau et al. in 2006,[2] (exhibiting a total turnover number (TON: $n(H_2)/n$(catalyst) of 238))[3] and its various derivatives, have been the subject of thorough investigation due to its promising photocatalytic properties.[4] Several experimental and theoretical investigations have explored how modifications to the bridging group[4a,c,5] and the catalytic centre[4c,d,6] affect the photophysical properties and the mechanistic pathways leading to catalytic activity.

The first step in the catalytic mechanism involves initial light-induced population of a singlet metal-to-ligand charge transfer (^{1}MLCT) state where an electron is donated from the ruthenium photosensitizer (PS) to the bridging ligand (BL), which acts an as electron relay and facilitates the electronic communication between the photocentre and the catalytic centre (CC). However, ^{1}MLCT states which populate vacant π* orbitals on the peripheral tbbpy co-ligands are also possible. Investigations of these systems revealed that there is an excitation wavelength dependence on the catalytic activity.[7] Quantum chemical and resonance Raman studies have shown that excitation to the blue end of the lowest energy absorption band populates the higher lying $^1MLCT_{(tbbpy)}$ states. Internal conversion can occur to then populate the $^1MLCT_{(BL)}$ state, but deactivation to the ground state is also possible, thereby reducing catalytic efficiency. Tuning the excitation to the red allows selective excitation of the $^1MLCT_{(BL)}$ state, from which further electron transfer processes towards the catalytic centre can take place and the $^1MLCT_{(tbbpy)}$ deactivation pathways are bypassed. Finally, the catalytic turn-over relies on complex processes among the excited states involving the three molecular building blocks namely the PS, the BL and the CC, with the desired outcome being forward electron transfer, resulting in the double reduction of the CC to enable photocatalytic H_2 generation.

In order to better direct the light-driven electron transfer onto a certain target ligand, e.g., a BL in photoactive dyads, we introduced an innovative, theory-driven design concept that utilizes electron rich peripheral bi(benz)imidazole (b(b)im) N,N-chelating co-ligands. As shown computationally, this approach allows the shifting of undesired ^{1}MLCT transitions involving these co-ligands to the ultraviolet spectral region, while simultaneously enhancing the electron storage capacity of the target ligand.[8] Subsequently, Rau and co-workers pursued this

[a] Dr. G. E. Shillito, Dr. S. Kupfer
Institute of Physical Chemistry
Friedrich Schiller University Jena
Helmholtzweg 4, 07743 Jena (Germany)
E-mail: stephan.kupfer@uni-jena.de
[b] Prof. Dr. S. Rau
Institute of Inorganic Chemistry I
Ulm University
Albert-Einstein-Allee 11, 89081 Ulm (Germany)

Supporting information for this article is available on the WWW under https://doi.org/10.1002/cctc.202201489

Special Collection

This publication is part of a Special Collection on "Photocatalytic Synthesis". Please check the ChemCatChem homepage for more articles in the collection.

strategy by incorporating such (b(b)im) ligands in $Ru^{II}(tbbpy)_2(N,N)$ complexes and demonstrated how such structural modification allows for the tuning of the excited state properties.[9] The non-chelating nitrogen atoms were protected by different alkyl groups, resulting in pH insensitivity, whereas the dianionic bim ligand would be readily protonated.[10] The high-lying $\pi_{b(b)im}$* orbitals of the bim-based ligands are largely inaccessible in the visible region and therefore direct electron transfer from the metal (PS) towards a target acceptor ligand with lower-lying π* orbitals. The complex possessing a N,N′-propylene-protected 1H, 1′H-2,2′ biimidazole (prbim) ligand demonstrated the best combination of excited state lifetime, photostability and no $Ru^{II}\rightarrow$prbim MLCT states in the visible region.[9] Orellana and co-workers also demonstrated that incorporation of a protonated bim ligand ($bimH_2$) in $[Ru(N,N)_2(bimH_2)]^{2+}$ complexes resulted in unidirectional MLCT transitions towards the (N,N) ligands in the visible region.[10b] Such ligand motifs can therefore steer light-driven electron transfer pathways towards a specific accepting ligand.

In the case of intramolecular photocatalysts, electron transfer should be directed towards the BL, from which further electron and/or energy transfer cascades occur to eventually reduce the CC, facilitating H_2 generation. The aim of the present quantum chemical study is to apply such bim-based ligands for the first time in catalytic active systems, i.e., in the scope of light-driven hydrogen generation. Herein we utilise quantum chemical simulations to investigate how a series of bim-based peripheral ligands affect the photophysical properties of $[(N,N)_2Ru(tpphz)RhCp^*Cl]^{n+/-}$ ($Cp^* = 1,2,3,4,5$-pentamethylcyclopentadiene) model complexes, as shown in Figure 1. The parent complex containing tbbpy co-ligands, $[(tbbpy)_2Ru(tpphz)RhCp^*Cl]^{3+}$ (TON = 17) was previously reported and its light-activated reaction mechanism elucidated by a joint synthetic-spectroscopic-theoretical approach.[11] Further investigation into the underlying electron transfer cascades in the forward (toward the CC), charge separation (CS) process, i.e. to activate the CC and enable photocatalytic H_2 production, are ongoing. Herein we examine the thermodynamics and kinetics

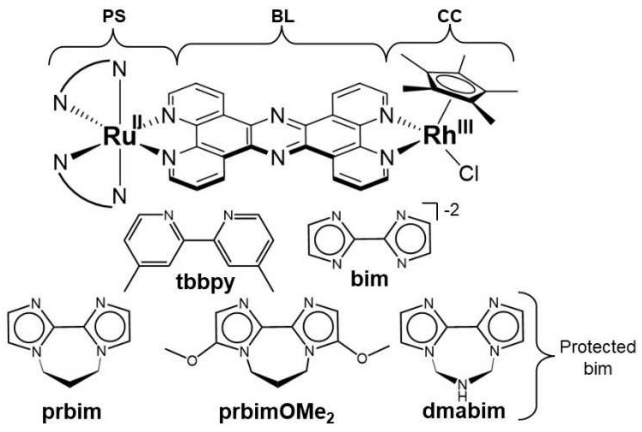

Figure 1. Structures of the investigated $[(N,N)_2Ru(tpphz)RhCp^*Cl]^{n+/-}$ complexes, with variation of the (N,N) ligand. PS, BL and CC correspond to the photosensitizer, bridging ligand and catalytic centre, respectively.

of a possible charge recombination (CR) pathway, directed back towards the PS, which therefore hinders catalytic activation in general.

We explore how peripheral ligand tuning affects the excited state properties in the Franck-Condon (FC) region and promotes unidirectional electron transfer, compared to the parent tbbpy species. Additionally, we investigate whether incorporation of such ligands could be a means by which to limit population of $^3MC_{(Ru)}$ states from the thermally equilibrated $^3MLCT_{(BL)}$ state, localised on the bridging ligand. Population of ^{3}MC states, which then rapidly non-radiatively decay to the ground state, represent a common deactivation pathway in d^6 metal complexes.[12] Tailoring the thermodynamic and kinetic accessibility of such undesirable excited state deactivation channels is therefore crucial to enhance the quantum efficiency as well as the catalytic turn-over. To this aim, the role of the co-ligands on this deactivating $^3MLCT(BL)\rightarrow{}^3MC(Ru)$ electron transfer pathway is examined using Marcus theory, in a similar manner to that reported for a related Ru-tpphz-Co complex.[13] Our design-approach towards limiting the deactivation pathway through ligand tuning could, in principle be applied to a broad range of PSs based on polypyridyl transition metal complexes, which would benefit from localising the excited state on a specific ligand, e.g. in the frame of light-harvesting, catalysis, sensing and photodynamic therapy.

Results and Discussion

Franck-Condon Photophysics

Quantum chemical calculations performed at the density and time-dependent density functional level of theory (DFT and TDDFT) predict that variation of the co-ligand has a significant effect on the complexes' electronic ground state properties, as well as on the photophysical properties in the Franck-Condon (FC) region. The FC geometries are similar for all the complexes, with Ru–N bond lengths of 2.1 Å and a symmetrical arrangement around the ruthenium centre, with bite angles of approximately 79° with each of the three coordinating ligands. Like the tpphz bridge, all the co-ligands are planar in the FC geometry, with dihedral angles close to 0°. Structural parameters are given in Table S1 and the equilibrium structures of the complexes may be accessed in Ref. [14].

Figure 2a depicts how the different co-ligands affect the energies of frontier molecular orbitals (FMOs) involved in the low-lying excited states of the studied complexes. Unsurprisingly, given the distance from the ancillary ligands, the FMOs of the bridging group and rhodium centre are largely unaffected by variation of the ligand. As anticipated, replacing the tbbpy ligand with the protected bim derivatives raises the energy of the respective π* acceptor orbitals with an increase of 0.87 eV observed from the tbbpy to prbim complex, with a small additional increase of 0.16 eV observed upon the addition of electron donating methoxy groups to the prbim ligands. The most notable changes are observed in the bim complex. This dianionic ligand is highly electron rich, raising the energy of the

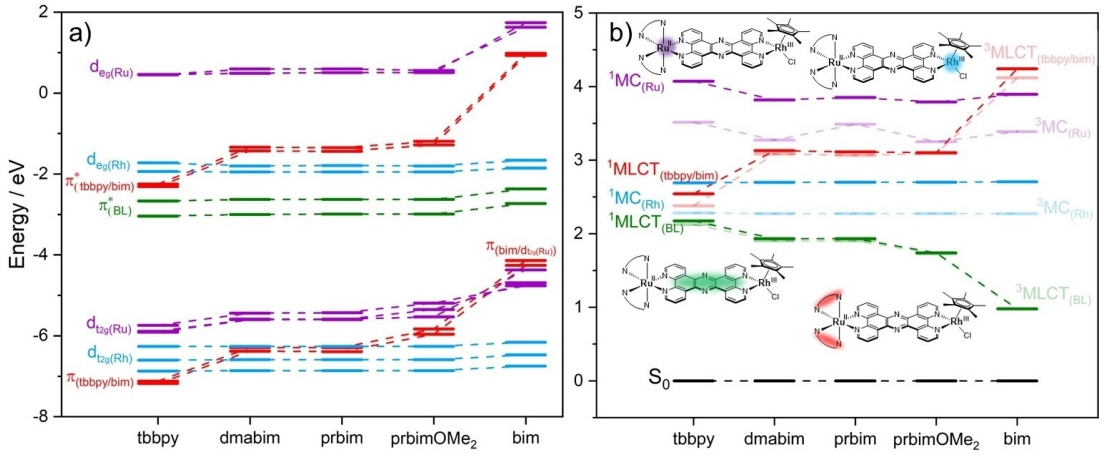

Figure 2. (TD)DFT predicted a) FMO energies and b) key singlet (solid bars) and triplet (faded bars) transition energies in the FC region as obtained at the TDDFT level of theory, for the complexes with varying (N,N) ligands. Co-ligand-based (π/π^*) orbitals are shown in red, π^* orbitals of the tpphz BL in green, and d orbitals of the Ru^{II} and the Rh^{III} centres in purple and blue, respectively. Electronic transitions in b) are colour-coded accordingly, while the electronic ground state (S_0) is shown in black.

occupied π_{bim} orbitals by ~3 eV relative to the π_{tbbpy}, causing this to mix with the d(Ru) orbitals, which also occurs to a lesser extent with the prbimOMe$_2$ complex (Table S2). This method of raising the π orbitals of the ligands sufficiently that they either mix with or are raised even above the metal d-orbitals in energy, in a processes dubbed 'HOMO inversion' has been reported previously in theory and experimental studies of Fe^{II} complexes.[15] The authors observed panchromatic absorption, nanosecond charge-transfer excited state lifetimes and destabilisation of the lowest lying MC states with respect to the ground state minimum.

The deprotonated bim ligand is highly electron rich and susceptible to protonation. A previous investigation of a $[Ru(bpy)_2(bimH_2)]^{2+}$ complex showed that F^- ions could be utilised to perform two-fold deprotonation of the ligand, with corresponding pK_a values of 7.2 and 12.1.[10a] Therefore the effects of protonation on the electronic properties of the Ru–Rh-based dyad containing singly and doubly protonated bim ligands were also explored. As shown in Figure S1, single and double protonation of each bim ligand (denoted bimH and bimH$_2$ respectively) causes the π_{bim} and π^*_{bim} orbitals, as well as the ruthenium t_{2g} and e_g orbitals to decrease in energy, becoming approximately isoenergetic with those of the prbim complex.

As illustrated in Figure 2b, the effects on the FMO energies translate to changes in the excited state energies. Most notably, as the co-ligands are changed from tbbpy, to the protected bim ligands, to the deprotonated bim, the $^1MLCT_{(BL)}$ and $^1MLCT_{(bpy/bim)}$ states are stabilised and destabilised, respectively. The same behaviour is predicted for the triplet state energies in the FC region (also see Figure S2). These effects can be observed in the simulated electronic absorption spectra shown in Figure 3. Key transitions are indicated with charge density difference (CDD) images, which depict how the electron density distribution changes during the transition, with the density moving from red to blue. Additional transitions and CDDs can be found in Table S3.

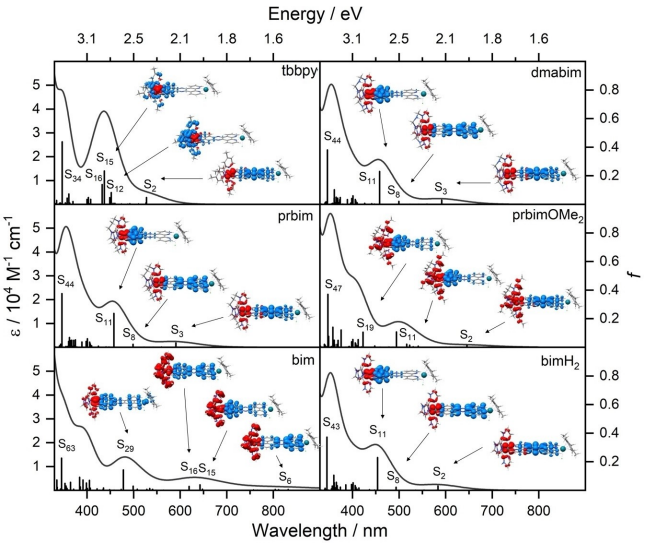

Figure 3. TDDFT predicted electronic absorption spectra of the complexes. Electronic transitions are shown with vertical bars, with the CDD images (electron density moving from red to blue) are used to depict the nature of key transitions.

TDDFT calculations predict that the tbbpy complex possesses a mixture of ^{1}MLCT states in the visible region, with electron density directed towards the bridge (S_2), the tbbpy ligands (S_{12}, S_{16}) and both ligand spheres (S_{15}). However, in the case of the protected bim complexes (prbim, prbimOMe$_2$ and dmabim), the visible region is dominated by unidirectional ^{1}MLCT transitions toward the bridging ligand, with the ^{1}MLCT transitions involving the ancillary ligands only predicted to occur at wavelengths shorter than ~400 nm. The same behaviour is also observed in the doubly protonated, bimH$_2$, which shows transitions of similar nature and energy to the

other protected bim species. In all cases, the UV region is dominated by intense ππ* transitions localised on the bridge.

The predicted electronic absorption spectrum of the deprotonated bim complex, exhibits the greatest hypsochromic shift relative to the tbbpy spectrum. Multiple ^{1}MLCT transitions span the entire visible region, all involving electron transfer to the bridge with no $^1MLCT_{(bim)}$ transitions occurring at wavelengths longer than 300 nm. This is in accordance with a previous computational investigation on a structurally related $(bim)_2Ru^{II}$-based PS.[8b] As stated above, the electron density on the deprotonated bim ligands is sufficiently high that they, as well as the ruthenium centre, function as donor groups. This can be readily seen in the CDD images in Figure 3, where significant contribution from the bim ligands as well as the metal is shown. A lesser contribution of electron density also occurs from the protected bim ligands in the other complexes.

Changing the tbbpy ligand for bim or a protected bim derivative, would thereby allow for increased spectator functionality, as the $^1MLCT_{(bim)}$ transition is pushed to sufficiently high energies (UV and near-UV region) to become inaccessible during Franck-Condon excitation. This is combined with stabilisation of the $^1MLCT_{(BL)}$ state, such that $^1MLCT_{(BL)}$ absorption is responsible for the majority of the signal intensity in the visible region, and whose population is the first step in the catalytic mechanism. Following (photo)reduction of the BL, forming $tpphz^{\bullet-}$, the electron must then be transferred to the catalytic centre. As modulation of the co-ligands surrounding the photocentre affects the energy of the π* orbitals of the BL, the reduction potentials of the catalytic centre may in turn need to be adjusted, such that the electron transfer process from $tpphz^{\bullet-}$ to Rh^{III}, reducing it to Rh^{II}, forming a CS state, can successfully occur. This could be achieved either by modification of the peripheral ligands of the catalyst or by selection of a different metal centre with a more suitably aligned reduction potential. Furthermore, two electron reduction or disproportionation, i.e. $2Rh^{II} \rightarrow Rh^{I} + Rh^{III}$, of the catalyst is required for H_2 generation.[16] An in-depth investigation into the mechanism involved in reduction of the catalytic centre will be addressed in future work and the CS and CR rates compared. Herein, a competitive CR pathway, whereby the photocatalyst is deactivated through population of a ^{3}MC state on the PS is explored.

Relaxed triplet manifold: Excited state deactivation

Following initial FC excitation into a $^1MLCT_{(BL)}$ state, rapid intersystem crossing occurs to populate a $^3MCLT_{(BL)}$ state.[11a] In order to promote catalytic activity, the electron needs to be transferred from the bridging group to the Rh^{III} centre, forming a CS state. However, competitive, deactivating, CR pathways also exist, one of which involves population of a ^{3}MC state on the ruthenium centre. Ideally, CS reaction pathways should proceed more quickly than the competing CR processes. By modulating the energy levels of the excited states in molecular photocatalysts, we aim to tune the kinetics of these pathways, increasing and decreasing the electron transfer rates for the competing CS and CR, respectively. Herein, the role that the co-ligand plays on the $^3MLCT_{(BL)}$ to $^3MC_{(Ru)}$ deactivation pathway is explored.

Within the Marcus picture, potential energy surfaces of the reactant (donor, D) and the product (acceptor, A) state are described as parabolas, while thermal fluctuation of the bath (e.g., solvent) introduce structural distortions that may lead to an electron transfer between the two diabatic states in the vicinity of their crossing. The electron transfer kinetics between the states of interest (D and A) are then governed by the reaction's driving force (ΔG), the reorganization energy (λ; inner sphere and outer-sphere effects) and by the electronic coupling between these states (H_{DA}). The Marcus parabola for the complexes containing tbbpy, dmabim and deprotonated bim co-ligands are presented in Figure 4, with the remaining data presented in Figure S3. The x-axis represents the one-dimensional (linear-interpolated internal) electron transfer coordinate connecting the optimised minima of the $^3MLCT_{(BL)}$ and $^3MC_{(Ru)}$ states, obtained at the DFT and TDDFT levels of theory; see computational details. This is represented visually by the vectors on the structures in Figure 4, which indicate the major structural changes occurring from the initial $^3MLCT_{(BL)}$ equilibrium geometry towards the final $^3MC_{(Ru)}$ geometry.

As depicted in Table S1, there are limited structural differences between the FC (S_0) and the $^3MLCT_{(BL)}$ geometries. However, the geometric changes accompanying the transition from the $^3MLCT_{(BL)}$ to the $^3MC_{(Ru)}$ state are more significant and primarily involve increasing the length of two of the Ru–N bonds in the plane of the tpphz ligand, from 2.1 to 2.4-2.8 Å. This increase in bond length is attributed to population of the antibonding $d_{x^2-y^2}$ (or rather σ*) orbital. In addition, in order to accommodate the increased bonds lengths, some twisting of the co-ligands occurs. This can be most clearly observed by examining the changes in angles between the different ligands and the metal centre. For example, in the $^3MLCT_{(BL)}$ geometry these angles are ~96°, close to the 90° expected for a perfectly octahedral structure. In the ^{3}MC geometries, however, the angle between each co-ligand and tpphz (illustrated in Table S1b) increases up to 108°, accompanied by a decrease in bite angle of each ligand, distorting the geometry to a similar extent for each complex. As stated previously, all co-ligands have an almost perfectly planar geometry in the S_0 and $^3MLCT_{(BL)}$ states, but in order to incorporate the increased Ru–N bond lengths in the ^{3}MC state, a slight increase in the dihedral angle of the co-ligands was observed, particularly in the case of the tbbpy complex, which increases from 0.6 to 10.9°.

The green and purple squares of Figure 4 represent the energies of the TDDFT (spin-forbidden singlet-triplet excitations) predicted $^3MLCT_{(BL)}$ and $^3MC_{(Ru)}$ states respectively, along the reaction coordinate, with additional, smaller interpolation steps made in the crossing region of both diabatic states. The points are fitted parabolically, to better illustrate the thermodynamic properties, i.e., driving force, ΔG, the donor and acceptor states' reorganisation energies, λ_D and λ_A and the crossing region where the photo-excited electron is transferred from the $^3MLCT_{(BL)}$ (D) to the $^3MC_{(Ru)}$ (A) state. This process corresponds to the electron, which is localised on the bridge in the $^3MLCT_{(BL)}$

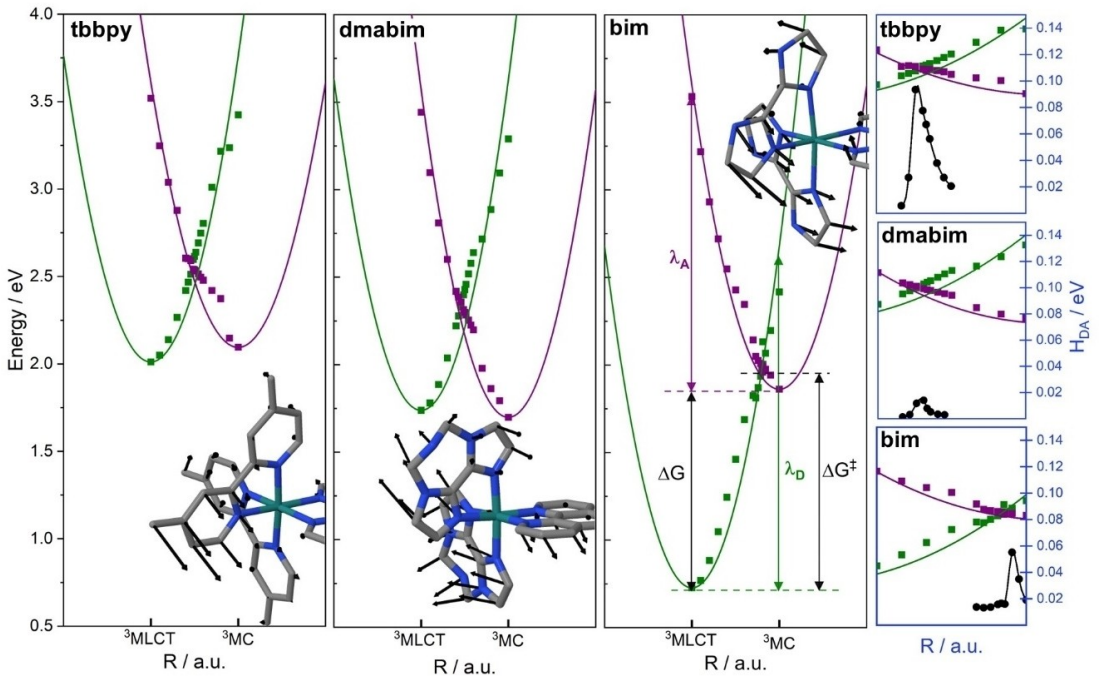

Figure 4. The left panels show the calculated diabatic potential energy surfaces of the $^3MLCT_{(BL)}$ (green) and $^3MC_{(Ru)}$ (purple) states along a linear-interpolated internal coordinate. The coordinates are indicted with displacement vectors, isolating the ruthenium centre for clarity. The energies were obtained at the TDDFT level of theory and fitted to a quadratic polynomial. The right panels show the energies of the diabatic states in the crossing region as well as the predicted electronic coupling values. To reduce computational time, the tbbpy ligands were modelled with CH_3 instead of tert-butyl groups.

state, being transferred to the vacant $d_{x^2-y^2}$ orbital on the ruthenium centre, i.e., into the lowest-lying $^3MC_{(Ru)}$ state.

In each case, the electron transfer process occurs in the Marcus normal region, as $-\Delta G < \lambda$. The co-ligand has an appreciable effect on the energies of the $^3MLCT_{(BL)}$ states, whereas the $^3MC_{(Ru)}$ states reside at a similar energy. This is likely attributed to a similar shift in both to occupied and unoccupied Ru(d) orbitals, as illustrated in Figure 2a. In the case of the dmabim and prbim complexes, ΔG is slightly exergonic, at −0.04 and −0.01 eV, respectively and slightly endergonic for the tbbpy and prbimOMe$_2$ complexes, at 0.08 and 0.15 eV, respectively. However, in the case of the deprotonated bim complex, ΔG is a very large positive value of 1.13 eV, accompanied by an activation energy of 1.22 eV and an average reorganisation energy of 1.68 eV. This implies that once the $^3MLCT_{(BL)}$ has been populated, the $^3MC_{(Ru)}$ pathway is effectively inaccessible. For the remaining complexes, Marcus theory was used to predict the electron transfer rates for the $^3MLCT_{(BL)} \rightarrow {}^3MC_{(Ru)}$ process. The electronic coupling (H_{DA}) was obtained by means of the Generalized Mulliken Hush approach (see Experimental Section, Equation 2) at different geometries in the crossing region, as shown in Figure 4 and the maximum value utilised. The H_{DA} values obtained range between merely 0.014 eV in case of the dmabim-modified dyad and 0.093 eV for the tbbpy parent compound. The three remaining systems (prbim, prbimOMe$_2$ and bim) feature couplings of approximately 0.05 eV. Thus, structural modification of the terminal co-ligand sphere does not only allow tuning of the thermodynamic properties of the unfavourable charge recombination, but also provides a means by which to tailor the underlying electronic coupling. As shown by our TDDFT simulations, the strongest – and thus least desirable – coupling is predicted for tbbpy, while all bim-based structures feature significantly smaller – and thus more favourable – H_{DA} values. All results are summarised in Table 1.

Subsequently, variation of the co-ligand affects the rate of electron transfer from the ^3MLCT to the $^3MC_{(Ru)}$ state, k_{et}. As shown in Figure 4 and Figure S3, the dmabim and prbim analogues are thermodynamically very similar to that of the parent tbbpy complex but have slower electron transfer rates for this undesirable $^3MLCT_{(BL)}$ to $^3MC_{(Ru)}$ CR process by 1–2 orders of magnitude. It should also be noted that the high degree of stabilisation of the $^3MLCT_{(BL)}$ state exhibited by the bim complex, while preventing deactivation of the complex through population of a $^3MC_{(Ru)}$ state, (i.e. $k_{et} \approx 0$) may give rise to additional deactivation channels. For example, based on the

Table 1. Comparison of the driving force ΔG, activation $\Delta G^{\ddagger}$ and average reorganisation energies of the donor and acceptor, λ_{av} ($\frac{\lambda_D+\lambda_A}{2}$) and electronic coupling H_{DA} values between the complexes. The rate constant, k_{et}, ($^3MLCT \rightarrow {}^3MC_{(Ru)}$) was obtained using Equation (1).

Ligand	ΔG [eV]	$\Delta G^{\ddagger}$ [eV]	λ_{av} [eV]	H_{DA} [eV]	k_{et} [s^{-1}]
tbbpy	0.08	0.45	1.42	0.093	1.91×10^7
dmabim	−0.04	0.46	1.65	0.014	5.17×10^5
prbim	−0.01	0.46	1.64	0.049	3.93×10^6
prbimOMe$_2$	0.15	0.54	1.67	0.040	6.93×10^4
bim	1.13	1.22	1.68	0.055	0

energy gap law, non-radiative decay to the ground state may rapidly occur due to the small S_0 to $^3MLCT_{(BL)}$ energy gap. Furthermore, as discussed previously, the corresponding energy levels of the CC would also need to be adjusted accordingly, such that the CS process, transferring the electron from the BL to reduce the CC can proceed. A highly basic environment would also be required to prevent protonation of the bim ligands,[17] which as previously discussed, causes the complex to behave similarly to the other protected bim species.

Previous theoretical investigations into the structurally similar complex, $[(bpy)_2Ru(tpphz)Co(bpy)_2]^{5+}$ revealed that the CR rates were 2–4 orders of magnitude slower than those for CS.[13] Furthermore, energy transfer mechanisms in complexes such as $[(tbbpy)_2Ru(tpphz)PdCl_2]^{2+}$ and $[(tbbpy)_2Ru(tpphz)PtCl_2]^{2+}$ as well as possible ligand loss at the CC appear, to play significant roles in the CS process.[4e,18] In order for such molecular systems to function as photocatalysts, two electrons must be acquired by the CC. The current investigation has focused on the transfer of a single electron to the BL, however, given the extensive destabilisation of the $MLCT_{(bim)}$ localised excited states observed in all bim based complexes, it is possible that the tpphz BL could accept an additional photo-induced electron. Quantum chemical investigations into the second electron transfer process will be addressed in future studies, as well as an investigation into the CS mechanism.

Conclusion

The photophysical properties of a series of potential molecular photocatalysts have been investigated using quantum chemical methods. Replacement of the tbbpy co-ligands of the parent complex with electron rich, bim based ligands, facilitates unidirectional charge transfer from the PS towards the BL in the visible region, thereby cutting off a potential deactivation pathway through population of MLCT states of the co-ligands. Following subsequent population of the $^3MLCT_{(BL)}$ state, Marcus analysis was utilised to determine the electron transfer rate for the undesirable, CR pathway to populate a $^3MC_{(Ru)}$ state. The driving force for this process is similar between the parent and protected bim complexes, yet the electronic coupling and rate of electron transfer is predicted to be notably slower for the protected bim complexes. The deprotonated, bim complex shows considerable stabilisation of the $^3MLCT_{(BL)}$ state, such that the $^3MC_{(Ru)}$ population becomes inaccessible, however such a significant stabilisation may open further deactivation pathways. Adjustment of the reduction potentials of the catalytic centre may be required in order to promote electron transfer from the $^3MLCT_{(BL)}$ state to reduce the catalytic centre.

This tuning methodology could be applicable to many standard polypyridyl-based transition metal compounds that would benefit from unidirectional excited state localisation, e.g., in the frame of light-harvesting, catalysis, sensing and photodynamic therapy. Currently, this strategy is under further investigation for structurally related photoactive dyads in a joint synthetic-spectroscopic-theoretical fashion, to explore the catalytic activation pathways. Simultaneously, alternative CCs are explored computationally to match the $^3MLCT_{(BL)}$ energy levels for the given set of bim based co-ligands to promote catalytic activity in the scope of photoinduced hydrogen production.

Experimental Section

All quantum chemical calculations were conducted using the Gaussian16 Program (Revision B.01).[19] Geometry optimisations to obtain relaxed structures, within both singlet and triplet manifolds were performed at the density functional level of theory (DFT) using the B3LYP functional with the split-valence def2svp basis set.[20] Grimme's D3 dispersion correction with Becke-Johnson damping was utilised to account for long-range interactions.[21] An implicit acetonitrile solvent field was incorporated with the integral equation formalism, utilising the SMD model.[22] Frequency calculations were performed on all optimised structures to verify that minima on the potential energy surface (PES) had been reached.

The excited state properties were investigated using time-dependent DFT (TDDFT) and the same XC functional and basis set as in case of the preceding ground state calculations. Several studies on structurally related photoactive transition metal complexes showed that such computational protocol enables an accurate prediction of ground and excited states properties with respect to experimental data, e.g. UV/vis absorption, resonance Raman spectra, (spectro-)electrochemical, transient absorption and electron transfer properties.[7c,13, 23] A balanced description of excited states featuring, i.e., metal-to-ligand charge transfer (MLCT), ligand-to-metal charge transfer (LMCT), ligand-to-ligand charge transfer (LLCT), intra-ligand charge transfer (ILCT) and metal-to-metal charge transfer (MMCT) in case of binuclear coordination compounds as well as intra-ligand (IL) and metal-centred (MC) character, as provided by the present computational setup, is essential to evaluate the rich photophysics of transition metal complexes. Vertical excitations were obtained from the optimised ground state singlet (S_0) and triplet state geometries, (T_{MLCT} and T_{MC}) for the 100 lowest singlet and the 100 lowest triplet states. The non-equilibrium solvent procedure was applied to the TDDFT excitation energies in the Franck-Condon region, such that only the fast electronic component of the solvent is equilibrated. To reduce computational time, the tbbpy ligands in the parent complex were modelled with CH_3 instead of tert-butyl groups. The optimised S_0, $^3MLCT_{(BL)}$ and $^3MC_{(Ru)}$ geometries of all complexes are available in Ref. [14] via the open data repository Zenodo.

The existence of multiple ^3MC states, in particular six low-lying states of $(t_{2g})^5$ $(e_g)^1$ nature, is well known in ruthenium complexes.[24] In the case of the investigated complexes, the ^3MC state utilised involved the $d_{x^2-y^2}$-like $d\sigma^*$ orbital of the ruthenium centre and was either the lowest (or approximately isoenergetic) ^3MC state that could be identified across the series of compounds (see Figure S6).

Electron transfer kinetics

The rate of electron transfer between the lowest energy $^3MLCT_{(BL)}$ state and a $^3MC_{(Ru)}$ state is modelled using semi-classical Marcus theory which can be applied to determine the non-adiabatic rate of electron transfer, k_{et} [Eq. (1)]. Thereby we follow our lately introduced protocol to assess the kinetics of intramolecular electron transfer processes along efficient reaction coordinates within the Marcus picture as benchmarked with respect to (dissipative) quantum dynamics.[4e,13,25] Very

recently, a similar approach for identifying such electron transfer coordinate by means of a linear combination of nuclear coordinates was presented by the Krewald group.[26] The potential energy surfaces of the donor ($^3MLCT_{(BL)}$) and acceptor ($^3MC_{(Ru)}$), states are modelled as parabola, displaced along a one-dimensional coordinate connecting the equilibrium geometries of the $^3MLCT_{(BL)}$ and $^3MC_{(Ru)}$ states and primarily involves distortion and elongation of bonds around the ruthenium core. Structural changes induced by thermal fluctuations may lead to electron transfer at the crossing point of the diabatic states, where ΔG is the driving force for electron transfer, λ is the reorganisation energy and T is the temperature (295 K).[27] H_{DA} corresponds to the maximum electronic coupling between the donor and acceptor. In summary, the electron transfer process corresponds to movement of the electron, localised on the bridge in the ^{3}MLCT 'donor' state (D), $[Ru^{III}(tpphz^{\bullet-})Rh^{III}Cp^*Cl]^{3+}$ back to the ruthenium centre (reducing it back to a Ru^{II} highspin species) into the antibonding $d_{x^2-y^2}$ orbital, forming the $^3MC_{(Ru)}$ 'acceptor' state (A). This deactivating process would hinder catalytic activity,[28] as it results in charge recombination on the ruthenium instead of accumulation of charge on the catalytic rhodium centre.

$$k_{et} = \frac{2\pi}{\hbar}|H_{DA}|^2(4\pi\lambda k_B T)^{-1/2}\exp\left(-\frac{(\Delta G+\lambda)^2}{4\lambda k_B T}\right) \quad (1)$$

To obtain the Marcus parabolas and the electron transfer kinetics, the one-dimensional reaction coordinate was obtained along a linear-interpolated internal coordinate connecting the optimised, equilibria geometries of the $^3MLCT_{(BL)}$ and $^3MC_{(Ru)}$ states. To this aim, our lately introduced external optimiser pysisyphus – also aware of excited states – was utilised.[29] Single point DFT as well as TDDFT calculations predicted energies to excited singlet and triplet states. These simulations were performed at each interpolated geometry, for both singlet and triplet species, allowing the energies of the ^{3}MLCT and ^{3}MC states to be obtained. Noteworthily, deexcitations do not contribute significantly to the electronic structure for the states of interest. Therefore, the Tamm-Dancoff approximation (TDA), which often provides an improved energetic description of the low-lying triplet states,[30] and TDDFT yield very similar excited state properties along the electron transfer coordinate as shown exemplarily for the tbbpy and the bim complexes (see Figures S4 and S5). Further interpolations were performed in the crossing region. The state energies were fitted using the simple polynomial function $E(R) = a(R-b)+c$ to guide the eye, where b and c correspond to the x and y axis offset of the parabola, respectively and were fixed based on the initial equilibrium geometry.

The Generalised Mulliken Hush approach, given in Equation (2),[31] was utilised in the interpolated geometries of the crossing region to determine the maximum H_{DA} between the two states. Equation (2) comprises the difference of the permanent dipole moments (μ_{ii}) of the two adiabatic states as well as of the transition dipole moment (μ_{ij}) between these two adiabatic states. ΔE is the energy difference between the (adiabat) ground and excited states.

$$H_{DA} = \frac{\mu_{12}\Delta E_{12}}{\sqrt{|\mu_{11}-\mu_{22}|^2+4|\mu_{12}|^2}} \quad (2)$$

As the states of interest (^{3}MLCT and ^{3}MC) are triplet in nature, the transition dipole moment between the lowest triplet state and the upper excited state, as well as the respective dipoles, were obtained from spin-allowed triplet-to-triplet TDDFT calculations in the crossing region, as the singlet-to-triplet transitions are spin-forbidden.

Acknowledgements

The authors thank Philipp Traber for initial simulations. Financial support by the Deutsche Forschungsgemeinschaft (DFG, German Research Foundation) – Projektnummer 448713509 as well as Projektnummer 364549901, TRR 234 [A1 and A4] – is gratefully acknowledged. Open Access funding enabled and organized by Projekt DEAL.

Conflict of Interest

The authors declare no conflict of interest.

Data Availability Statement

The data that support the findings of this study are openly available in Zenodo at https://doi.org/10.5281/zenodo.7318770, reference number 14.

Keywords: TDDFT · electron transfer · Marcus theory · molecular photocatalysts

[1] a) T. Stoll, M. Gennari, J. Fortage, C. E. Castillo, M. Rebarz, M. Sliwa, O. Poizat, F. Odobel, A. Deronzier, M.-N. Collomb, *Angew. Chem. Int. Ed.* **2014**, *53*, 1654–1658; *Angew. Chem.* **2014**, *126*, 1680–1684; b) T. J. Whittemore, C. Xue, J. Huang, J. C. Gallucci, C. Turro, *Nat. Chem.* **2020**, *12*, 180–185; c) Y.-J. Yuan, Z.-T. Yu, D.-Q. Chen, Z.-G. Zou, *Chem. Soc. Rev.* **2017**, *46*, 603–631; d) J. Corredor, M. J. Rivero, C. M. Rangel, F. Gloaguen, I. Ortiz, *J. Chem. Technol. Biotechnol.* **2019**, *94*, 3049–3063.
[2] S. Rau, B. Schäfer, D. Gleich, E. Anders, M. Rudolph, M. Friedrich, H. Görls, W. Henry, J. G. Vos, *Angew. Chem. Int. Ed.* **2006**, *45*, 6215–6218; *Angew. Chem.* **2006**, *118*, 6361–6364.
[3] M. Karnahl, C. Kuhnt, F. Ma, A. Yartsev, M. Schmitt, B. Dietzek, S. Rau, J. Popp, *ChemPhysChem* **2011**, *12*, 2101–2109.
[4] a) M. G. Pfeffer, C. Müller, E. T. E. Kastl, A. K. Mengele, B. Bagemihl, S. S. Fauth, J. Habermehl, L. Petermann, M. Wächtler, M. Schulz, D. Chartrand, F. Laverdière, P. Seeber, S. Kupfer, S. Gräfe, G. S. Hanan, J. G. Vos, B. Dietzek-Ivanšić, S. Rau, *Nat. Chem.* **2022**, *14*, 500–506; b) Q. Pan, L. Freitag, T. Kowacs, J. C. Falgenhauer, J. P. Korterik, D. Schlettwein, W. R. Browne, M. T. Pryce, S. Rau, L. González, J. G. Vos, A. Huijser, *Chem. Commun.* **2016**, *52*, 9371–9374; c) M. Lämmle, S. Volk, M. Klinkerman, M. Müßler, A. K. Mengele, S. Rau, *Photochemistry* **2022**, *2*, 831–848; d) M. G. Pfeffer, B. Schäfer, G. Smolentsev, J. Uhlig, E. Nazarenko, J. Guthmuller, C. Kuhnt, M. Wächtler, B. Dietzek, V. Sundström, S. Rau, *Angew. Chem. Int. Ed.* **2015**, *54*, 5044–5048; *Angew. Chem.* **2015**, *127*, 5132–5136; e) M. Staniszewska, S. Kupfer, J. Guthmuller, *Chem. Eur. J.* **2018**, *24*, 11166–11176.

[5] a) C. Kuhnt, M. Karnahl, S. Rau, M. Schmitt, B. Dietzek, J. Popp, *Chem. Phys. Lett.* **2011**, *516*, 45–50; b) L. Zedler, P. Wintergerst, A. K. Mengele, C. Müller, C. Li, B. Dietzek-Ivanšić, S. Rau, *Nat. Commun.* **2022**, *13*, 2538.
[6] M. G. Pfeffer, L. Zedler, S. Kupfer, M. Paul, M. Schwalbe, K. Peuntinger, D. M. Guldi, J. Guthmuller, J. Popp, S. Gräfe, B. Dietzek, S. Rau, *Dalton Trans.* **2014**, *43*, 11676–11686.
[7] a) M. Wächtler, J. Guthmuller, S. Kupfer, M. Maiuri, D. Brida, J. Popp, S. Rau, G. Cerullo, B. Dietzek, *Chem. Eur. J.* **2015**, *21*, 7668–7674; b) S. Tschierlei, M. Karnahl, M. Presselt, B. Dietzek, J. Guthmuller, L. González, M. Schmitt, S. Rau, J. Popp, *Angew. Chem. Int. Ed.* **2010**, *49*, 3981–3984; *Angew. Chem.* **2010**, *122*, 4073–4076; c) L. Zedler, J. Guthmuller, I. Rabelo de Moraes, S. Kupfer, S. Krieck, M. Schmitt, J. Popp, S. Rau, B. Dietzek, *Chem. Commun.* **2014**, *50*, 5227–5229.
[8] a) L. Zedler, S. Kupfer, I. R. de Moraes, M. Wächtler, R. Beckert, M. Schmitt, J. Popp, S. Rau, B. Dietzek, *Chem. Eur. J.* **2014**, *20*, 3793–3799; b) S. Kupfer, *Phys. Chem. Chem. Phys.* **2016**, *18*, 13357–13367.
[9] A. K. Mengele, C. Müller, D. Nauroozi, S. Kupfer, B. Dietzek, S. Rau, *Inorg. Chem.* **2020**, *59*, 12097–12110.
[10] a) Y. Cui, H.-J. Mo, J.-C. Chen, Y.-L. Niu, Y.-R. Zhong, K.-C. Zheng, B.-H. Ye, *Inorg. Chem.* **2007**, *46*, 6427–6436; b) J. Quílez-Alburquerque, C. García-Iriepa, M. Marazzi, A. B. Descalzo, G. Orellana, *Inorg. Chem.* **2022**, *61*, 328–337.
[11] a) L. Zedler, A. K. Mengele, K. M. Ziems, Y. Zhang, M. Wächtler, S. Gräfe, T. Pascher, S. Rau, S. Kupfer, B. Dietzek, *Angew. Chem. Int. Ed.* **2019**, *58*, 13140–13148; *Angew. Chem.* **2019**, *131*, 13274–13282; b) A. K. Mengele, S. Kaufhold, C. Streb, S. Rau, *Dalton Trans.* **2016**, *45*, 6612–6618.
[12] a) A. Soupart, I. M. Dixon, F. Alary, J.-L. Heully, *Theor. Chem. Acc.* **2018**, *137*, 37; b) S. Cerfontaine, S. A. M. Wehlin, B. Elias, L. Troian-Gautier, *J. Am. Chem. Soc.* **2020**, *142*, 5549–5555; c) Y. Liu, K. S. Kjær, L. A. Fredin, P. Chábera, T. Harlang, S. E. Canton, S. Lidin, J. Zhang, R. Lomoth, K.-E. Bergquist, P. Persson, K. Wärnmark, V. Sundström, *Chem. Eur. J.* **2015**, *21*, 3628–3639.
[13] A. Koch, D. Kinzel, F. Dröge, S. Gräfe, S. Kupfer, *J. Phys. Chem. C* **2017**, *121*, 16066–16078.
[14] G. E. Shillito, **2022**; DFT optimised structures of Ru(II)-based photocatalysts; Zenodo; DOI: 10.5281/zenodo.7318770.
[15] a) S. Mukherjee, D. E. Torres, E. Jakubikova, *Chem. Sci.* **2017**, *8*, 8115–8126; b) J. D. Braun, I. B. Lozada, C. Kolodziej, C. Burda, K. M. E. Newman, J. van Lierop, R. L. Davis, D. E. Herbert, *Nat. Chem.* **2019**, *11*, 1144–1150; c) J. D. Braun, I. B. Lozada, D. E. Herbert, *Inorg. Chem.* **2020**, *59*, 17746–17757.
[16] U. Kölle, B.-S. Kang, P. Infelta, P. Comte, M. Grätzel, *Chem. Ber.* **1989**, *122*, 1869–1880.
[17] a) S. Rau, T. Büttner, C. Temme, M. Ruben, H. Görls, D. Walther, M. Duati, S. Fanni, J. G. Vos, *Inorg. Chem.* **2000**, *39*, 1621–1624; b) S. Rau, M. Ruben, T. Büttner, C. Temme, S. Dautz, H. Görls, M. Rudolph, D. Walther, A. Brodkorb, M. Duati, C. O'Connor, J. G. Vos, *J. Chem. Soc. Dalton Trans.* **2000**, 3649–3657.
[18] M. Staniszewska, S. Kupfer, J. Guthmuller, *J. Phys. Chem. C* **2019**, *123*, 16003–16013.
[19] M. J. Frisch, G. W. Trucks, H. B. Schlegel, G. E. Scuseria, M. A. Robb, J. R. Cheeseman, G. Scalmani, V. Barone, G. A. Petersson, H. Nakatsuji, X. Li, M. Caricato, A. V. Marenich, J. Bloino, B. G. Janesko, R. Gomperts, B. Mennucci, H. P. Hratchian, J. V. Ortiz, A. F. Izmaylov, J. L. Sonnenberg, D. Williams-Young, F. Ding, F. Lipparini, F. Egidi, J. Goings, B. Peng, A. Petrone, T. Henderson, D. Ranasinghe, V. G. Zakrzewski, J. Gao, N. Rega, G. Zheng, W. Liang, M. Hada, M. Ehara, K. Toyota, R. Fukuda, J. Hasegawa, M. Ishida, T. Nakajima, Y. Honda, O. Kitao, H. Nakai, T. Vreven, K. Throssell, J. J. A. Montgomery, J. E. Peralta, F. Ogliaro, M. J. Bearpark, J. J. Heyd, E. N. Brothers, K. N. Kudin, V. N. Staroverov, T. A. Keith, R. Kobayashi, J. Normand, K. Raghavachari, A. P. Rendell, J. C. Burant, S. S. Iyengar, J. Tomasi, M. Cossi, J. M. Millam, M. Klene, C. Adamo, R. Cammi, J. W. Ochterski, R. L. Martin, K. Morokuma, O. Farkas, J. B. Foresman, D. J. Fox, Gaussian 16, Gaussian Inc., Wallingford CT, **2016**.
[20] F. Weigend, R. Ahlrichs, *Phys. Chem. Chem. Phys.* **2005**, *7*, 3297–3305.
[21] S. Grimme, S. Ehrlich, L. Goerigk, *J. Comput. Chem.* **2011**, *32*, 1456–1465.
[22] A. V. Marenich, C. J. Cramer, D. G. Truhlar, *J. Phys. Chem. B* **2009**, *113*, 6378–6396.
[23] a) J. Guthmuller, L. González, *Phys. Chem. Chem. Phys.* **2010**, *12*, 14812–14821; b) L. González, D. Escudero, L. Serrano-Andrés, *ChemPhysChem* **2012**, *13*, 28–51; c) C. Latouche, D. Skouteris, F. Palazzetti, V. Barone, *J. Chem. Theory Comput.* **2015**, *11*, 3281–3289; d) D. Escudero, *Transition Metals in Coordination Environments*, *1st ed.*, Springer Cham, **2019**.
[24] a) K. Eastham, P. A. Scattergood, D. Chu, R. Z. Boota, A. Soupart, F. Alary, I. M. Dixon, C. R. Rice, S. J. O. Hardman, P. I. P. Elliott, *Inorg. Chem.* **2022**, *61*, 19907–19924; b) L. Hammarström, O. Johansson, *Coord. Chem. Rev.* **2010**, *254*, 2546–2559-2546–2559; c) I. M. Dixon, E. Lebon, P. Sutra, A. Igau, *Chem. Soc. Rev.* **2009**, *38*, 1621–1634-1621–1634.
[25] a) M. Richter, B. P. Fingerhut, *J. Chem. Phys.* **2017**, *146*, 214101; b) M. Richter, B. P. Fingerhut, *Faraday Discuss.* **2019**, *216*, 72–93; c) C. Zens, C. Friebe, U. S. Schubert, M. Richter, S. Kupfer, *ChemSusChem* **2022**, e202201679.
[26] A. Šrut, B. J. Lear, V. Krewald, **2022**, ChemRxiv preprint DOI: 10.26434/chemrxiv-2022-253hc.
[27] a) R. A. Marcus, *J. Chem. Phys.* **1956**, *24*, 966–978; b) R. A. Marcus, *Annu. Rev. Phys. Chem.* **1964**, *15*, 155–196; c) R. A. Marcus, P. Siddarth, *Photoprocesses in Transition Metal Complexes, Biosystems and Other Molecules.* Experiment and Theory, Springer, **1992**, pp. 49–88; d) R. A. Marcus, N. Sutin, *Biochim. Biophys. Acta Rev. Bioenerg.* **1985**, *811*, 265–322.
[28] a) A. T. Yeh, C. V. Shank, J. K. McCusker, *Science* **2000**, *289*, 935–938; b) S. Cerfontaine, L. Troian-Gautier, S. A. M. Wehlin, F. Loiseau, E. Cauët, B. Elias, *Dalton Trans.* **2020**, *49*, 8096–8106.
[29] J. Steinmetzer, S. Kupfer, S. Gräfe, *Int. J. Quantum Chem.* **2021**, *121*, e26390.
[30] a) M. J. G. Peach, M. J. Williamson, D. J. Tozer, *J. Chem. Theory Comput.* **2011**, *7*, 3578–3585; b) P. Kumar, D. Escudero, *Inorg. Chem.* **2021**, *60*, 17230–17240.
[31] a) J. Zheng, Y. K. Kang, M. J. Therien, D. N. Beratan, *J. Am. Chem. Soc.* **2005**, *127*, 11303–11310; b) R. J. Cave, M. D. Newton, *Chem. Phys. Lett.* **1996**, *249*, 15–19; c) J. E. Subotnik, S. Yeganeh, R. J. Cave, M. A. Ratner, *J. Chem. Phys.* **2008**, *129*, 244101; d) R. J. Cave, M. D. Newton, *J. Chem. Phys.* **1997**, *106*, 9213–9226; e) M. Rust, J. Lappe, R. J. Cave, *J. Phys. Chem. A* **2002**, *106*, 3930–3940.

Manuscript received: November 29, 2022
Revised manuscript received: January 5, 2023
Accepted manuscript online: January 9, 2023
Version of record online: January 20, 2023